A DISTANCE DRIVEN METHOD FOR METAL ARTEFACT REDUCTION IN COMPUTED TOMOGRAPHY

Andre Mouton[*], *Najla Megherbi*[*], *Katrien Van Slambrouck*[+], *Johan Nuyts*[+], *Toby P. Breckon*[*]
[*]School of Engineering, Cranfield University, Bedfordshire, UK.
[+] Dept. Nuclear Medicine and Medical Imaging Research Centre, KU Leuven, Belgium

ABSTRACT

This paper presents an extension to a recent intensity-limiting sinogram completion-based Metal Artefact Reduction (MAR) algorithm for Computed Tomography (CT) images containing multiple metal objects. A novel weighting scheme is introduced, whereby the intensities of the MAR-corrected pixels are modified based on their spatial locations relative to the metal objects. Pixels falling within the straight-line regions connecting multiple metal objects are subjected to less intensive intensity-limiting, thereby compensating for the characteristic dark bands occurring in these regions. Extensive experimentation is performed on a state-of-the-art numerical simulation, a clinical CT data set and a baggage security CT data set. Comprehensive performance analysis, using reference and reference-free error metrics, Bland-Altman plots and visual comparisons, demonstrate an improvement in the restoration of the underestimated intensities occurring in the regions connecting multiple metal objects.

Index Terms— metal artefact reduction, CT, baggage CT

1. INTRODUCTION

Metal artefacts can corrupt X-ray Computed Tomography (CT) images so severely that they become extremely challenging to interpret and of limited usability (see Fig. 1). In X-ray CT, the most widely implemented reconstruction technique, in both clinical and industrial practices, is the Filtered Back-Projection (FBP) algorithm. The FBP algorithm is based on an analytical inversion of the Radon transform [1] and yields fast and accurate reconstructions from ideal (or near-ideal) projections, which contain a sufficient number of projection samples and low degrees of noise, beam hardening and any other imperfections [2]. In the presence of high-density objects, such as metals, however, the effects of beam hardening, scattered radiation, photon starvation, noise and the partial volume effect cause the FBP algorithm to produce reconstructions characterised by dark shadows and intense streaks, making the interpretation of the regions connecting and surrounding the metal objects challenging [3].

Several Metal Artefact Reduction (MAR) techniques exist. The majority of these techniques fall into one of three categories: sinogram (or projection) completion methods; iterative methods and hybrid methods. Sinogram completion-based approaches consider the projections going through the metal objects as corrupted and replace the corresponding projection data using interpolation techniques (e.g. linear [4] or spline [5] interpolation). The corrected sinograms are reconstructed via FBP, yielding images with reduced streaking. Such techniques are generally straightforward to implement and involve minimal computational overhead, making them a popular choice. Iterative reconstruction methods allow for the introduction of prior information and statistical models to more accurately model the acquisition process. Iterative methods generally yield superior reconstructions compared to Filtered Back Projection, especially in the presence of incomplete and/or corrupted projection data. Despite the development of optimised approaches [6, 7, 8, 9, 10, 11, 12], high computational cost remains the major factor preventing the universal implementation of such techniques in commercial CT machines.

Direct interpolation-based sinogram completion approaches generally perform adequately when only a single, small metal object is present in the Field-of-View (FoV). Muller and Buzug [13] have demonstrated that the biggest disadvantage of sinogram correction by direct interpolation is that all edge information (i.e. not just metal object edges) lying on the beams passing through the metal objects is lost. Sinogram correction by this so-called 'naive interpolation' ultimately leads to the generation of secondary streaks in the corrected images [3, 13]. Furthermore, in the presence of multiple metal objects, dark bands often appear between pairs of metal objects due to unequal quantities of beam hardening across views [14].

Several MAR techniques have been proposed to better preserve edge and contrast information, thereby reducing the generation of secondary artefacts when dealing with images containing multiple metal objects. Pre- and post-filtering techniques [15, 16], feedback strategies [17], guided sinogram completion techniques based on priors obtained via multiclass segmentation [13, 18, 19, 20, 21], wavelet techniques [22, 23], Fourier-based interpolation [24] and region-specific interpolation [15, 16] have been proposed and met with varying degrees of success. With the exception of [16], these methods are all intended for use in the medical field. In the medical domain, prior information regarding the contents (i.e. anatomical composition) and nature (e.g. attenuation profiles) of the CT scans is available. This prior information allows for effective parameter tuning and can be used to 'guide' the interpolation process [3]. Those MAR techniques that rely on effective parameter tuning and/or prior information [13, 18, 19, 20, 21, 22, 23] are however, expected to be of limited value in the security screening domain, where the contents of the scans are inherently unpredictable making the generation of prior information and effective parameter tuning more challenging.

We recently proposed a novel, yet efficient, interpolation-based MAR approach for the reduction of metal artefacts in CT baggage security imagery [16]. The method yielded a performance improvement when compared to algorithms based on linear interpolation [4] and reprojection-reconstruction [15] and has been shown to perform comparably to state-of-the-art MAR methods in extensive experimentation [25]. The approach however, performs poorly in image regions corrupted by dark bands: a phenomenon which typically occurs in the regions connecting multiple metal objects. In this study, we propose a modification to our earlier work and demonstrate an improvement in performance for both medical and baggage CT imagery.

2. PROPOSED ALGORITHM

Mouton *et al.* [16] presented a MAR technique for CT baggage imagery composed of the following steps:

1. Metal segmentation: Metallic objects present in the original reconstructed image are segmented by binary thresholding, yielding a 'metal-only' image. A 'metal-free' image is then constructed by assigning a constant pixel value to the metallic regions in the original, reconstructed image. The metal-free image is filtered with the

Funded under the Innovative Research Call in Explosives and Weapons Detection (2010), sponsored by Home Office Scientific Development Branch, Dept. for Transport, Centre for the Protection of National Infrastructure and Metro. Police Service. The authors thank Reveal Imaging Technologies Inc. (USA) for additional support.

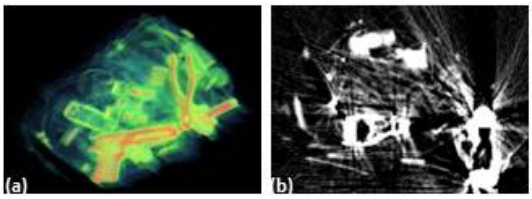

Fig. 1. (a) Volumetric baggage CT scan. (b) 2D axial slice from volume in (a) displaying streaking artefacts.

edge preserving Non-Local Means (NLM) filter [26] to reduce weak streaking artefacts and background noise while preserving the non-metallic regions of the image.

2. Reprojection and sinogram completion: The metal-only image and the filtered, metal-free image are forward projected using the Radon transform [27], yielding the corresponding sinograms. The metal-only sinogram is used to index the bins in the metal-free sinogram that are to be replaced by spline-interpolation.

3. Image reconstruction: The interpolated sinogram is reconstructed via Filtered Back-Projection (FBP) [27] to obtain the corrected, metal-free image. The metal objects are then reinserted into the interpolated image, yielding the corrected image.

4. Image refinement: The pixel values in the corrected image are limited to be less than or equal to the corresponding pixels in the original image to remove the secondary streaking resulting from the interpolation process. To eliminate the remaining weak streaks, the image is again filtered with the NLM filter [26].

The image refinement step is motivated by the fact that the secondary streaks introduced by the interpolation procedure generally manifest as intense, bright lines affecting the entire image. Regions previously unaffected by streaking, but exhibiting secondary streaks, are thus characterised by higher pixel values (see yellow regions in FBP and Kalender images Figs. 4 and 5). By imposing an upper limit on the corrected pixel values, much of the secondary streaking is eliminated. Further experimentation [25] however, has revealed a limitation in this reasoning. In images containing multiple metallic objects, a common manifestation of unequal beam-hardening across views [3], is the appearance of dark bands (underestimated attenuation values) in the straight-line regions connecting the metal objects (see Fig. 2). While the sinogram completion approach generally yields adequate correction of such regions, this correction is undone by the image refinement step in [16]. Considering that the approach in [16] was developed for use in the security CT domain, it is likely that this limitation was overlooked due to the typically high dynamic range of security CT images [28, 29]. Such high dynamic ranges result in naturally dark background regions [16, 30, 31], thereby making dark bands inherently less prominent. Applying the technique to medical CT imagery, where windowing is used to improve the visibility of low-density anatomy, has emphasised this shortcoming [25].

To address this limitation, we replace the aforementioned refinement technique with a distance-weighted refinement procedure, whereby the degree of intensity limiting is dependent on the location of the pixels relative to the metal objects. Particularly, pixels falling within the straight-line regions connecting two metal objects are subjected to less intensive intensity refinement. For every pair of metal objects, a set of 'refinement weights' are computed in the following way (illustrated in Fig. 2):

1) The centroid of each metal object is determined (red 'x' in Fig. 2). **2)** For the smaller of the two metal objects (Metal 1 in Fig. 2), an ellipse having the same second-moments as the metal object is determined. **3)** The angle that the line passing through the centroids makes with the horizontal is computed and compared to the angles that the major and minor axes of the ellipse make with the horizontal. **4)** The width of the weight-mask is set to the length of the

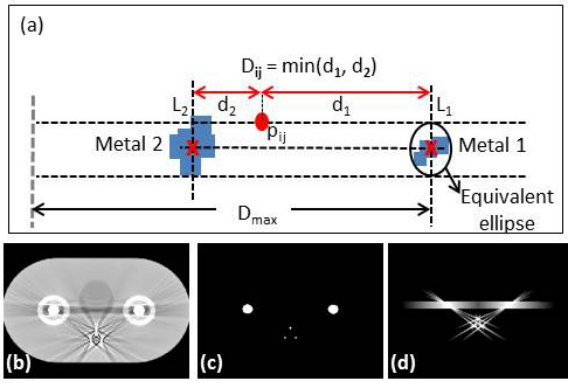

Fig. 2. (a) Illustration of the weighted mask generation. The intensity refinement of pixel p_{ij} is dependent on the distance to the nearest metal object. The width of the mask is equal to the width of the ellipse surrounding the smaller of the two objects (Metal 1). (b) Example input image (c) Multiple metal objects (d) Resulting weighted mask.

ellipse axis which is nearest in orientation to the line connecting the centroids. **5)** The weights (in the range [0, 1]) are computed based on the Euclidean distance from the mask pixel to the nearest of the two metal objects such that pixels nearer to metal objects have higher weights. For a pixel $\mathbf{p} = (p_i, p_j)$ in the mask located at (i, j) on a rectangular image grid, the corresponding weight $w(i_j)$ is computed as follows:

$$w(i,j) = \frac{|D(i,j) - D_{max}|}{D_{max}} \tag{1}$$

$$D(i,j) = \min\{D(\mathbf{p}, L_1), D(\mathbf{p}, L_2)\} \tag{2}$$

where $D(\mathbf{p}, L)$ is the perpendicular Euclidean distance between the pixel $\mathbf{p}$ at image location (i, j) and the straight line L; $L_{1,2}$ are the straight lines passing through the centroids of the two metal objects, perpendicular to the line connecting the two centroids; D_{max} is the distance by which the mask extends beyond each metal object and is a tunable parameter (see Fig. 2). For every pixel outside of the mask, $w(i, j)$ is set to zero. **6)** For a pixel $\mathbf{p} = (p_i, p_j)$ the refined intensity $I(i, j)$ is then computed as follows:

$$I(i,j) = [1 - w(i,j)] \cdot I_0 + w(i,j) \cdot I_c \tag{3}$$

where I_c is the corrected intensity value of the pixel (i.e. after Step 3. in the aforementioned algorithm) and I_0 is the original (uncorrected) pixel intensity.

3. METHODOLOGY

It is common practice in the medical literature to use numerical simulations and mathematical phantoms to measure the performance of MAR techniques, as this allows for reliable quantitative performance analysis [12, 17, 32, 33, 34, 35].

We use a 2D phantom composed of two large circular iron inserts (diameter 2 cm) surrounded by circles of cancellous (soft) bone; three small isolated circular iron inserts (diameter 0.4 cm) and a region of fatty tissue. The remainder of the phantom is composed of water. The numerical simulation of the phantom was performed using a state-of-the-art simulator based on that presented by De Man *et al.* [3], extended with a distance driven projector [36]. This 2D simulator has been used extensively in previous MAR studies [3, 12, 32, 34, 35]. The simulation models the effects of beam hardening (due to the polychromatic nature of X-ray spectra), scattered radiation, projection noise and the trans-axial non-linear partial volume effect. De Man *et al.* [3] have cited these as the predominant causes of streaking in medical CT images. The simulation includes a 10-times subsampling of the detector elements, a 5-times subsampling of the source (using a source width of 1 mm) and a 5-times

subsampling of the projection views (to model the continuous rotation of the gantry). The effects of afterglow and detector-crosstalk were not considered. Scatter is simulated according to the following formula:

$$s_i = F_0 \cdot C_c \cdot y_i \cdot \ln(b_i/y_i) \quad (4)$$

where s_i is the scatter value at position i in the sinogram and i indicates both the angle and position (within the detector array) of the projection line; F_0 is the fraction of photons scattered forward (at an angle of 0^o); C_c is the fraction of the attenuation resulting from Compton scatter (i.e. electron-photon interactions); y_i is the transmission simulation value at i and $\ln(b_i/y_i)$ is the log-converted sinogram (b_i is the blank scan value representing the detected number of photons in sinogram pixel i in the absence of an absorber).

A fan-beam acquisition was simulated using 672 detectors and 1160 views per rotation (360°). We used a focus-to-isocentre distance of 570 mm, a focus-to-detector distance of 1040 mm, a Field of View (FoV) diameter of 50 cm and a detector angular aperture of 0.0774° (these geometric parameters approximate the Siemens SOMATOM Sensation 64 CT scanner). A simulated X-ray spectrum was generated using the Xcomp5 software [37] at a nominal tube voltage of 140 kV. After simulation, the fan-beam sinograms were rebinned to parallel beam data [38]. Filtered Back Projection (FBP) was used to create the reconstructed image with 512 x 512 pixels. The final, artefact corrupted simulation is illustrated in Fig. 2 (a). To allow for quantitative analysis, a reference image was generated using an identical polychromatic simulation but without metal inserts.

Furthermore, a spiral CT scan (see Fig. 4) of a patient with a double hip prosthesis is used as clinical test data. The spiral CT data was acquired on a Siemens Sensation 16 system as part of a Biograph16 PET/CT scanner (Siemens Medical Solutions, Knoxville, TN) at a nominal tube voltage of 120 kVp, a Computed Tomography Dose Index (CTDI) of 11.9, using a collimation of 16 x 1.5 mm. A reconstruction slice thickness of 3 mm was used. Prior to reconstruction, the spiral data was rebinned to parallel beam data [38].

The MAR method in [16] was initially intended for use in the aviation security screening domain. We thus include a data set composed of 12 volumetric baggage CT scans (e.g. Fig. 1) obtained using the CT-80 model dual-energy baggage scanner (Reveal Imaging Inc.). A fan-beam geometry was employed with a focus-to-isocentre distance of 550 mm, a focus-to-detector distance of 1008.4 mm at a nominal tube voltage of 160 kVp. The optimal spatial resolution of the scanner is 1.56x1.61x5.00mm. Prior to reconstruction, the fan-beam sinograms were rebinned to parallel beam data [38]. The volumetric baggage scans contain multiple metallic objects (firearms, belt buckles, metallic zippers etc.) in cluttered environments. We consider all non-metallic objects in the scan as clutter and these include a variety of commonly encountered objects of varying density (e.g. clothing, bottles etc.).

Quantitative performance analysis for the simulated data is performed by computing the Normalised Root Mean Squared Error (NRMSE) [39, 40] of the difference between the FBP-reconstructed image without metal inserts and the MAR-corrected image:

$$\text{NRMSE} = \sqrt{\frac{\sum_{j=1}^{\tilde{N}}(f_j - f_j^{ref})^2}{\sum_{j=1}^{\tilde{N}}(f_j^{ref} - \mu)^2}} \quad (5)$$

where f_j is the corrected image; f_j^{ref} is the reference image; μ is the mean of all the reference image intensities and $\tilde{N}$ is the (reduced) number of pixels in the image (as the regions corresponding to the metal inserts are not considered).

For the patient and baggage CT data (where no ground-truth is available), quantitative analysis is performed using the reference-free error metric of Kratz *et al.* [41] which utilises the raw projection data outside of the metal trace as ground-truth data. The Normalised Reference-Free Errors (denoted as NRFE) are represented as a factor of the unprocessed (FBP) error (a value of 1 would correspond to no improvement). Two individual 2D axial CT slices (1 baggage slice and 1 patient slice), exhibiting significant streaking artefacts, are used for these error analyses.

The patient and baggage CT data are subjected to further quantitative analysis using Bland-Altman plots [42]. The Bland-Altman plot considers the mean intensities in three types of image regions before and after MAR: 1) overestimated regions (pixel densities higher than expected due to artefacts); 2) underestimated regions (pixel densities lower than expected due to artefacts) and 3) unaffected regions (pixels unaffected by streaking). In each individual 2D axial CT slice obtained from the clinical data as well as selected axial slices obtained from the 12 volumetric baggage scans, 5 ROIs are manually specified (2 overestimated, 2 underestimated and 1 unaffected). Two measurements are made for every ROI: 1) the mean intensity of the ROI before MAR and 2) the mean intensity of the ROI after MAR. The Bland-Altman plot then plots the difference of the two ROI measurements as a function of their mean. Successful MAR should yield a decrease in the mean intensity of the overestimated regions, an increase in the underestimated regions and little/no change in the unaffected regions.

4. RESULTS

The performance of the proposed MAR method (denoted as Mou_β) was compared to that of our earlier approach [16] (denoted as Mou_α) for each data set, using the aforementioned analysis techniques. The Mou_α approach has previously been shown to perform comparably to several state-of-the-art methods in [16, 25], but for the sake of completeness, the performance of the linear interpolation-based MAR approach of Kalender *et al.* [4] (denoted as Kalender) is included in the error and qualitative performance comparisons.

Table 1 shows the Normalised Root Mean Squared Errors (NRMSEs) for the simulated data and the Normalised Reference-Free Errors (NRFEs) for the patient and baggage data. As demonstrated in our earlier work [16], the Mou_α approach yields a reduction in error compared to both the unprocessed (FBP) image as well as the linear interpolation approach of Kalender [4] in all three scenarios. More significantly, the Mou_β approach has resulted in a 13.6% decrease in error in the simulated image, a 24.3% decrease in error in the patient image and an 11.5% decrease in error in the baggage image.

Figs. 3 - 5 show the qualitative results for the images used in the above error analyses. As expected, the Mou_α and Mou_β approaches yielded significant reductions in streaking (compared to the FBP image) and further produced superior images compared to the Kalender approach. At first glance, the Kalender image in Fig. 3 appears to be of good quality with very little streaking. Upon closer inspection (magnified images on the right in Fig. 3) however, a loss in edge and contrast information is apparent. This deterioration in image quality is not evident in the $\text{Mou}_{\alpha,\beta}$ images. While a similar blurring is evident in the patient and baggage Kalender images (Figs. 4 and 5), the images are further corrupted by secondary streaks - especially evident in the background regions. The regions marked in yellow in Fig. 4 illustrate where the Kalender image contains secondary streaking and the $\text{Mou}_{\alpha,\beta}$ images are free of streaking. The yellow regions in Fig. 5 show streaks in the FBP image which the $\text{Mou}_{\alpha,\beta}$ methods removed but the Kalender method did not. The magnified images in each of the Figs. 3 - 5, further demonstrate the superior performance of the Mou_β approach in regions containing dark bands. While the improvements for the simulated (Fig. 3) and patient images (Fig. 4) are significant, they are less obvious in the

Method	NRMSE (phantom)	NRFE (patient)	NRFE (baggage)
FBP	0.872	1.00	1.00
Kalender	0.401	0.460	0.537
Mou_α	0.221	0.238	0.259
Mou_β	0.191	0.180	0.229

Table 1. Quantitative error analysis results for phantom, patient and baggage experiments.

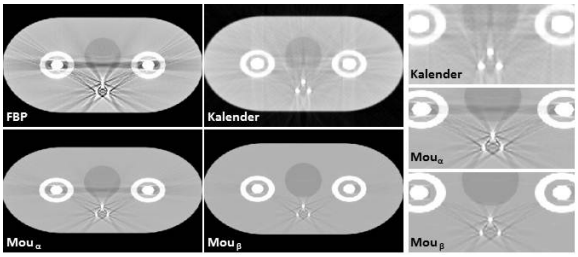

Fig. 3. Qualitative analysis results for phantom data. The magnified images on the right show a more detailed comparison of performance. Window = 800 HU, Centre = 0 HU

baggage image (Fig. 5). The underestimated regions in the baggage data are, however, inherently more difficult to identify to the naked-eye due to the high dynamic range of the images. Nonetheless, the magnifications in Fig. 5 display a noticeable increase in the intensity in the region between the two high density objects (marked in red).

Figs. 6 and 7 show the BlandAltman plots generated from the uncorrected and corrected CT data for the patient and baggage data sets respectively. The overestimated (OE), underestimated (UE), and unaffected (UA) regions in each data set are represented using different coloured markers. The graphs for both experiments confirm the desired modifications to the image intensities in the overestimated (yellow markers) and unaffected regions (red markers) after MAR. Since the Mou_β approach only modifies the behaviour of the Mou_α approach in the regions connecting metal objects, the two approaches give the same results for the overestimated and unaffected regions. As desired, for both the patient (Fig. 6) and baggage data (Fig. 7) the readings in the overestimated regions are consistently in the positive portions of the graphs (along the vertical axes), indicating a reduction in the overestimated intensities after MAR. Furthermore, for both data sets, the readings in the unaffected regions are closely clustered around the horizontal axes, indicating little to no change in the image intensities after MAR. The green and blue markers display the behaviour of the Mou_α and Mou_β approaches respectively in the underestimated regions and clearly demonstrate the improvement achieved by the proposed modifications to the Mou_α approach. While the Mou_α approach yielded readings clustered around the horizontal axes (indicating little/no change in the intensities after MAR), the Mou_β readings in both experiments consistently occurred in the negative vertical portions of the graphs - indicating a successful increase in the underestimated intensities.

The results in the quantitative and qualitative analyses confirm that the proposed modifications to the intensity limiting MAR technique of Mouton *et al.* [16] lead to improved metal artefact reduction in CT images containing multiple metal objects.

5. CONCLUSIONS

This study presents an extension to the intensity limiting CT-MAR approach of Mouton *et al.* [16] (previously proven against the state-of-art [16, 25]). A weighting scheme is introduced into the intensity limiting process, whereby the location of pixels relative to metal objects are considered. Subsequently, less intensive intensity limiting is applied in the straight line regions connecting multiple metal objects, thereby better compensating for the characteristic underestimated attenuation coefficients in these regions. Comprehensive experimentation, using both clinical and simulated medical CT data as well as cluttered baggage CT data has shown a significant quantitative as well as qualitative improvement in performance.

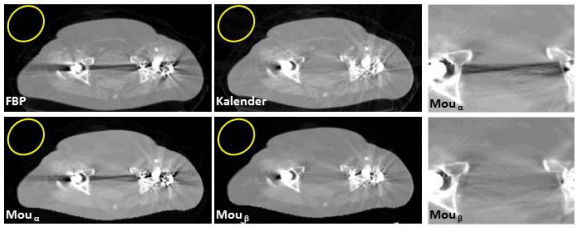

Fig. 4. Qualitative analysis results (with magnifications on the right) for patient data. The regions marked in yellow show where linear interpolation (Kalender) has resulted in secondary streaking and $\text{Mou}_{\alpha,\beta}$ have not. Window = 500 HU, Centre = 0 HU

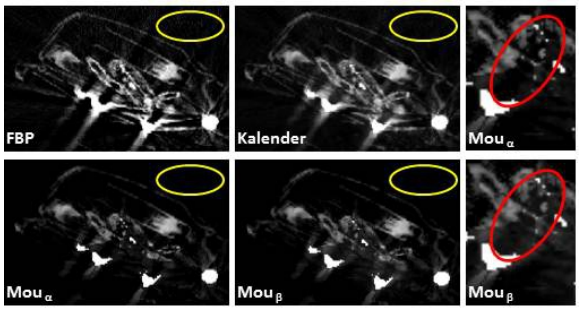

Fig. 5. Qualitative analysis results (with magnifications on the right) for baggage data. The regions marked in yellow show where linear interpolation (Kalender) has failed to remove streaking and $\text{Mou}_{\alpha,\beta}$ have succeeded.

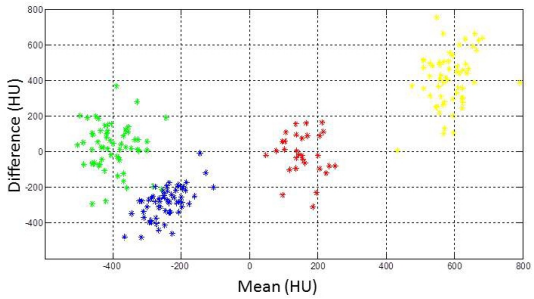

Fig. 6. Bland-Altman plot for clinical data. Yellow = overestimated; red = unaffected; green = underestimated (Mou_α); blue = underestimated (Mou_β).

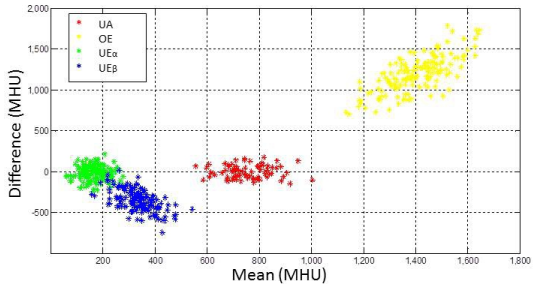

Fig. 7. Bland-Altman plot for baggage data using Modified Hounsfield Units (MHU). Yellow = overestimated; red = unaffected; green = underestimated (Mou_α); blue = underestimated (Mou_β).

6. REFERENCES

[1] Stanley R. Deans, *The Radon Transform and Some of Its Applications*, Krieger Publishing Company, 1993.

[2] J. Hsieh, *Computed tomography: principles, design, artifacts, and recent advances*, SPIE and John Wiley and Sons, 2003.

[3] B. De Man, J. Nuyts, P. Dupont, G. Marchal, and P. Suetens, "Metal streak artifacts in x-ray computed tomography: a simulation study," in *IEEE Trans. on Nuclear Science*, 1999, vol. 46, pp. 691–696.

[4] W. A. Kalender, R. Hebel, and J. Ebersberger, "Reduction of CT artifacts caused by metallic implants.," *Radiology*, vol. 164, no. 2, pp. 576, 1987.

[5] M. Abdoli, M. R. Ay, A. Ahmadian, and H. Zaidi, "A virtual sinogram method to reduce dental metallic implant artefacts in computed tomography-based attenuation correction for pet," *Nuclear medicine communications*, vol. 31, no. 1, pp. 22, 2010.

[6] H. M. Hudson and R. S. Larkin, "Accelerated image reconstruction using ordered subsets of projection data," *IEEE Trans. on Medical Imaging*, vol. 13, no. 4, pp. 601–609, 1994.

[7] J. Browne and A. B. de Pierro, "A row-action alternative to the EM algorithm for maximizing likelihood in emission tomography," *IEEE Trans. on Medical Imaging*, vol. 15, no. 5, pp. 687–699, 1996.

[8] Z. Yu, J. B. Thibault, C. A. Bouman, K. D. Sauer, and J. Hsieh, "Fast model-based X-Ray CT reconstruction using spatially nonhomogeneous ICD optimization," *IEEE Trans. on Image Processing*, vol. 20, no. 1, pp. 161–175, 2011.

[9] C. L. Byrne, "Convergent block-iterative algorithms for image reconstruction from inconsistent data," *Image Processing, IEEE Trans. on*, vol. 6, no. 9, pp. 1296–1304, 1997.

[10] Q. Li, S. Ahn, and R. Leahy, "Fast hybrid algorithms for PET image reconstruction," in *Nuclear Science Symposium Conference Record, IEEE*, 2005, vol. 4, pp. 1851–1855.

[11] F. E. Boas and D. Fleischmann, "Evaluation of two iterative techniques for reducing metal artifacts in computed tomography," *Radiology*, vol. 259, no. 3, pp. 894–902, 2011.

[12] B. De Man, J. Nuyts, P. Dupont, G. Marchal, and P. Suetens, "Reduction of metal streak artifacts in X-ray computed tomography using a transmission maximum a posteriori algorithm," *IEEE Trans. on Nuclear Science*, vol. 47, no. 3, pp. 977–981, 2000.

[13] J. Muller and T.M. Buzug, "Spurious structures created by interpolation-based CT metal artifact reduction," in *Proc. of SPIE*, 2009, vol. 7258, p. 72581Y.

[14] J. F. Barrett and N. Keat, "Artifacts in CT: Recognition and avoidance," *Radiographics*, vol. 24, no. 6, pp. 1679–1691, 2004.

[15] K. Y. Jeong and J. B. Ra, "Reduction of artifacts due to multiple metallic objects in computed tomography," in *Proc. SPIE*, 2009, vol. 7258, p. 72583E.

[16] A. Mouton, N. Megherbi, G.T. Flitton, and T.P. Breckon, "A novel intensity limiting approach to metal artefact reduction in 3D CT baggage imagery," in *IEEE Inter. Conf. on Image Processing*, 2012, pp. 2057–2060.

[17] H. Yu, K. Zeng, D. K. Bharkhada, G. Wang, M. T. Madsen, O. Saba, B. Policeni, M. A. Howard, and W. R. K. Smoker, "A segmentation-based method for metal artifact reduction," *Academic Radiology*, vol. 14, no. 4, pp. 495–504, 2007.

[18] E. Meyer, R. Raupach, M. Lell, B. Schmidt, and M. Kachelriess, "Normalized metal artifact reduction (NMAR) in computed tomography," *Medical physics*, vol. 37, pp. 5482, 2010.

[19] E. Meyer, R. Raupach, B. Schmidt, A. H. Mahnken, and M. Kachelriess, "Adaptive normalized metal artifact reduction (ANMAR) in computed tomography," in *Nuclear Science Symposium and Medical Imaging Conference (NSS/MIC), 2011 IEEE*, 2011, pp. 2560–2565.

[20] E. Meyer, R. Raupach, M. Lell, B. Schmidt, and M. Kachelriess, "Frequency split metal artifact reduction (FSMAR) in computed tomography," *Medical physics*, vol. 39, no. 4, pp. 1904–1916, Apr 2012.

[21] Seemeen Karimi, Pamela Cosman, Christoph Wald, and Harry Martz, "Segmentation of artifacts and anatomy in CT metal artifact reduction," *Medical Physics*, vol. 39, no. 10, pp. 5857–5868, 2012.

[22] S. Zhao, D. D. Robeltson, G. Wang, B. Whiting, and K. T. Bae, "X-ray CT metal artifact reduction using wavelets: an application for imaging total hip prostheses," *IEEE Trans. on Medical Imaging*, vol. 19, no. 12, pp. 1238–1247, 2000.

[23] S. Zhao, K. T. Bae, B. Whiting, and G. Wang, "A wavelet method for metal artifact reduction with multiple metallic objects in the field of view," *Journal of X-Ray Science and Technology*, vol. 10, no. 2, pp. 67–76, 2002.

[24] B. Kratz, T. Knopp, J. Muller, M. Oehler, and T. M. Buzug, "Non-equispaced Fourier Transform vs. polynomial-based metal artifact reduction in computed tomography," *Bildverarbeitung fur die Medizin*, pp. 21–25, 2008.

[25] A. Mouton, N. Megherbi, K. van Slambrouk, J. Nuyts, and T.P. Breckon, "An experimental survey of metal artefact reduction in computed tomography," *Journal of X-Ray Science and Technology*, vol. 21, no. 2, pp. 193–226, 2013.

[26] A. Buades, B. Coll, and J. M. Morel, "On image denoising methods," *SIAM Multiscale Modeling and Simulation*, vol. 4, no. 2, pp. 490–530, 2005.

[27] A. F. Kopp, K. Klingenbeck-Regn, M. Heuschmid, A. Kuttner, B. Ohnesorge, T. Flohr, S. Schaller, and C. D. Claussen, "Multislice computed tomography: basic principles and clinical applications," *Electromedica-Erlangen*, vol. 68, no. 2, pp. 94–105, 2000.

[28] N. Megherbi, G. T. Flitton, and T. P. Breckon, "A classifier based approach for the detection of potential threats in CT based baggage screening," in *ICIP*, 2010, pp. 1833–1836.

[29] G. Flitton, T.P. Breckon, and N. Megherbi, "Object recognition using 3D SIFT in complex CT volumes," in *Proc. British Machine Vision Conference*, 2010, pp. 11.1–11.12.

[30] Y. Zhou, K. Panetta, and S. Agaian, "CT baggage image enhancement using a combination of alpha-weighted mean separation and histogram equalization," in *Proc. SPIE*, 2010, vol. 7708, p. 77080G.

[31] A. Mouton, N. Megherbi, G.T. Flitton, and T.P. Breckon, "An evaluation of ct image denoising techniques applied to baggage imagery screening," in *IEEE Inter. Conf. on Industrial Technology*, 2013, to appear.

[32] B. De Man, J. Nuyts, P. Dupont, G. Marchal, and P. Suetens, "An iterative maximum-likelihood polychromatic algorithm for CT," *IEEE Trans. on Medical Imaging*, vol. 20, no. 10, pp. 999–1008, 2001.

[33] B. De Man, *Iterative Reconstruction for Reduction of Metal Artifacts in Computed Tomography [PhD Thesis]*, Ph.D. thesis, Katholieke Universiteit Leuven, 2001.

[34] C. Lemmens, D. Faul, and J. Nuyts, "Suppression of metal artifacts in CT using a reconstruction procedure that combines MAP and projection completion," *IEEE Trans. on Medical Imaging*, vol. 28, no. 2, pp. 250–260, 2009.

[35] K. Van Slambrouck and J. Nuyts, "Metal artifact reduction in computed tomography using local models in an image block-iterative scheme," *Medical physics*, vol. 39, no. 11, pp. 7080, 2012.

[36] B. De Man and S. Basu, "Distance-driven projection and backprojection in three dimensions," *Physics in Medicine and Biology*, vol. 49, no. 11, pp. 2463, 2004.

[37] R. Nowotny and A. Hfer, "Program for calculating diagnostic x-ray spectra," *RoFo: Fortschritte auf dem Gebiete der Rontgenstrahlen und der Nuklearmedizin*, vol. 142, no. 6, pp. 685, 1985.

[38] L. Wang, "Cross-section reconstruction with a fan-beam scanning geometry," *IEEE Trans. on Computers*, vol. 100, no. 3, pp. 264–268, 1977.

[39] R. S. Brock, A. Docef, and M. J. Murphy, "Reconstruction of a cone-beam CT image via forward iterative projection matching," *Medical physics*, vol. 37, no. 12, pp. 6212, 2010.

[40] G. T. Herman, *Fundamentals of computerized tomography: image reconstruction from projections*, Springer, 2009.

[41] B. Kratz, S. Ens, J. Mller, and T. M. Buzug, "Reference-free ground truth metric for metal artifact evaluation in CT images," *Medical Physics*, vol. 38, pp. 4321–4328, 2011.

[42] D.G. Altman and J.M. Bland, "Measurement in medicine: the analysis of method comparison studies," *The Statistician*, vol. 32, pp. 307–317, 1983.